Miro1-mediated mitochondrial positioning shapes intracellular energy gradients required for cell migration

Max-Hinderk Schuler[a], Agnieszka Lewandowska[a], Giuseppe Di Caprio[b,c], Wesley Skillern[b,c], Srigokul Upadhyayula[b,c], Tom Kirchhausen[b,c,d,*], Janet M. Shaw[a,*], and Brian Cunniff[b,c,†,*]

[a]Department of Biochemistry, University of Utah School of Medicine, Salt Lake City, UT 84112; [b]Program in Cellular and Molecular Medicine, Boston Children's Hospital, Boston, MA 02115; [c]Department of Cell Biology and [d]Department of Pediatrics, Harvard Medical School, Boston, MA 02115

ABSTRACT It has long been postulated, although never directly demonstrated, that mitochondria are strategically positioned in the cytoplasm to meet local requirements for energy production. Here we show that positioning of mitochondria in mouse embryonic fibroblasts (MEFs) determines the shape of intracellular energy gradients in living cells. Specifically, the ratio of ATP to ADP was highest at perinuclear areas of dense mitochondria and gradually decreased as more-peripheral sites were approached. Furthermore, the majority of mitochondria were positioned at the ventral surface of the cell, correlating with high ATP:ADP ratios close to the ventral membrane, which rapidly decreased toward the dorsal surface. We used cells deficient for the mitochondrial Rho-GTPase 1 (Miro1), an essential mediator of microtubule-based mitochondrial motility, to study how changes in mitochondrial positioning affect cytoplasmic energy distribution and cell migration, an energy-expensive process. The mitochondrial network in *Miro1*^{−/−} MEFs was restricted to the perinuclear area, with few mitochondria present at the cell periphery. This change in mitochondrial distribution dramatically reduced the ratio of ATP to ADP at the cell cortex and disrupted events essential for cell movement, including actin dynamics, lamellipodia protrusion, and membrane ruffling. Cell adhesion status was also affected by changes in mitochondrial positioning; focal adhesion assembly and stability was decreased in *Miro1*^{−/−} MEFs compared with *Miro1*^{+/+} MEFs. Consequently *Miro1*^{−/−} MEFs migrated slower than control cells during both collective and single-cell migration. These data establish that Miro1-mediated mitochondrial positioning at the leading edge provides localized energy production that promotes cell migration by supporting membrane protrusion and focal adhesion stability.

INTRODUCTION

Cell migration is required for numerous physiological and pathophysiological processes, including development, wound healing, immune response, and cancer metastasis (Trepat *et al.*, 2012). The process is organized via signaling events that coordinate lamellipodia protrusion, focal adhesion dynamics, and tail retraction to actively move the cell forward (Ridley *et al.*, 2003; Zaidel-Bar *et al.*, 2004). Actin branching, kinase activation, and membrane reorganization during cell migration all consume energy at the leading edge, which was recently proposed to arise from mitochondrial sources (Cunniff *et al.*, 2016).

Mitochondria are dynamic organelles that vary in size, shape, and location, depending on cell type, state, and metabolic demand

(Soubannier and McBride, 2009). In mammalian cells, mitochondria are the primary source of cellular energy in the form of ATP, actively buffer calcium (Ca^{2+}), and produce reactive oxygen species as a by-product of aerobic respiration (McBride et al., 2006; Osellame et al., 2012). The shape and distribution of the mitochondrial network are partly controlled by cellular cues that respond to changes in energy needs (Liesa and Shirihai, 2013), Ca^{2+} transients (Cai and Sheng, 2009; Niescier et al., 2013; Schwarz, 2013), and posttranslational modifications (Soubannier and McBride, 2009). Network distribution is facilitated by microtubule-associated molecular motors—kinesin and dynein—which move individual mitochondria along microtubule tracks (Tanaka et al., 1998; Hollenbeck and Saxton, 2005; Pilling et al., 2006). Mitochondrial coupling to kinesin and dynein is mediated by a protein complex consisting of TRAK1/2 and the mitochondrial Rho GTPases 1 and 2 (Miro1/2; Stowers et al., 2002; Fransson et al., 2003, 2006; Brickley et al., 2005; Guo et al., 2005; Glater et al., 2006). Miro1 is a C-terminal–anchored mitochondrial outer membrane protein that contains two GTPase and two EF-hand ligand mimic (ELM) domains (Fransson et al., 2003; Frederick et al., 2004; Klosowiak et al., 2013, 2016). Each ELM domain consists of a canonical and a hidden Ca^{2+}-binding EF hand, which are stabilized by a ligand-mimic domain (Klosowiak et al., 2013, 2016). Ca^{2+} binding to the canonical EF hands halts mitochondrial transport in neurons, positioning mitochondria at sites of high-energy demand (Saotome et al., 2008; MacAskill et al., 2009; Wang and Schwarz, 2009).

The intracellular localization of mitochondria has become an active area of research because of its importance in immune function (Campello et al., 2006; Quintana and Hoth, 2012; Morlino et al., 2014), neurological activity (Cai et al., 2011; Saxton and Hollenbeck, 2012; Schwarz, 2013), response to cell stress (Al-Mehdi et al., 2012; Liesa and Shirihai, 2013; Hoppins, 2014), and, most recently, cell migration (Wang et al., 2011; Desai et al., 2013; Zhao et al., 2013; Caino et al., 2015; Rivadeneira et al., 2015; Cunniff et al., 2016). Increased mitochondrial bioenergetics and distribution to the cortical cytoskeleton are associated with tumor cell migration and invasion (Zhao et al., 2013; Caino et al., 2015; Rivadeneira et al., 2015). Moreover, orientation of the mitochondrial network anterior to the direction of cell migration correlates with persistent movement of breast cancer cells during chemotaxis in microfluidic channels (Desai et al., 2013), and recent evidence suggests that the leading edge is fueled by mitochondrial, rather than glycolytic, ATP (Cunniff et al., 2016). In this context, the AMP-activated protein kinase regulates mitochondrial redistribution to the cortical cytoskeleton, supporting increased energy demands during cell migration and three-dimensional (3D) invasion (Cunniff et al., 2016). Nevertheless, how mitochondrial positioning at the leading edge of nontumorigenic cells influences intracellular energy levels and cell migration remains unclear.

Here we provide direct evidence that the intracellular location of mitochondria shapes subcellular energy gradients. When visualized by live-cell spinning-disk confocal and 3D fluorescence lattice light sheet microscopy (LLSM), control cells expressing Miro1 displayed a shallow ATP:ADP gradient extending outward from the perinuclear region to the cell periphery and from the basal to the dorsal surface. Restriction of the mitochondrial network to the perinuclear area in cells lacking Miro1 steepened the intracellular ATP:ADP gradient, with the highest ATP:ADP ratios directly adjacent to the dense mitochondrial mass around the nucleus. Changes in intracellular energy distribution were associated with impaired leading-edge protrusion, membrane ruffling, and focal adhesion dynamics in Miro1$^{-/-}$ mouse embryonic fibroblasts (MEFs), resulting in decreased cell migration rates. Together these results

demonstrate that cytoplasmic positioning of functional mitochondria is critical for localized energy production during energy-consuming processes underlying cell migration.

RESULTS AND DISCUSSION

Perinuclear restriction of mitochondria in Miro1$^{-/-}$ MEFs alters intracellular energy status

As reported previously, deletion of Miro1 restricts the mitochondrial network to the perinuclear space (Figure 1A) without affecting mitochondrial bioenergetics (Nguyen et al., 2014). To confirm that mitochondria from Miro1$^{-/-}$ MEFs are bioenergetically healthy, we performed Seahorse Extracellular Flux analysis on Miro1$^{+/+}$ and Miro1$^{-/-}$ MEF clones (Figure 1B and Supplemental Figure S1). Basal and maximal oxygen consumption rates (OCRs) were only mildly elevated in Miro1$^{-/-}$ MEFs compared with Miro1$^{+/+}$ MEFs (Figure 1, B–D). Similarly, the spare reserve capacity of Miro1$^{-/-}$ MEFs was only slightly increased compared with Miro1$^{+/+}$ MEFs, indicating that Miro1$^{-/-}$ MEFs maintain the capacity to respond to increased energy demands (Figure 1E). These data indicate that mitochondrial respiratory chain function was largely unaffected by deletion of Miro1 (Divakaruni et al., 2014; Nguyen et al., 2014).

We next measured ATP and ADP levels in whole-cell lysates collected from Miro1$^{+/+}$ and Miro1$^{-/-}$ MEFs (Figure 1, F–H). Whereas ATP levels were comparable between both genetic backgrounds (Figure 1F), ADP levels were elevated in Miro1$^{-/-}$ MEFs (Figure 1G), leading to a reduced ATP:ADP ratio (Figure 1H). This increase in intracellular ADP levels in Miro1$^{-/-}$ MEFs may result from higher ATP consumption at perinuclear sites (Jones, 1986) and may also explain the mildly elevated basal and maximal OCRs observed by Seahorse Extracellular Flux analysis in Miro1$^{-/-}$ MEFs, because elevated intracellular ADP levels stimulate mitochondrial respiration (Berg et al., 2002). Together our data indicate that loss of Miro1 alters the intracellular energy status but does not impair mitochondrial bioenergetics in MEFs. Thus Miro1$^{-/-}$ MEFs provide an ideal system to quantify changes specifically caused by defects in mitochondrial positioning.

In situ determination of 3D energy gradients in living cells

Using live-cell imaging of Miro1$^{+/+}$ and Miro1$^{-/-}$ MEFs transiently expressing mitochondrial-targeted green fluorescent protein (mito-GFP) and the mCherry-tagged actin-binding protein LifeAct (Riedl et al., 2008), we observed a constant flux of mitochondria infiltrating the leading edge of Miro1$^{+/+}$ MEFs (Figure 1I and Supplemental Movie S1). By contrast, we observed no directional mitochondrial movement in Miro1$^{-/-}$ MEFs (Figure 1J and Supplemental Movie S1). We next asked whether positioning of healthy mitochondria influenced subcellular energy levels, an idea that has been proposed but never documented by direct imaging in living cells (Niethammer et al., 2008; Jayashankar and Rafelski, 2014). To visualize the subcellular energy status in Miro1$^{+/+}$ and Miro1$^{-/-}$ MEFs, we used 3D fluorescence spinning-disk confocal microscopy to follow the ATP:ADP biosensor PercevalHR (Berg et al., 2009; Tantama et al., 2013; Figure 2A). Binding of ATP or ADP to PercevalHR increases the fluorescence signal emitted at 540 nm after excitation with either 488- or 405 nm light, respectively. The ratio of the emitted signals provides a relative measurement of local energy levels that is independent of protein concentration, expression level, and fluorophore bleaching (Berg et al., 2009; Tantama et al., 2013). In Miro1$^{+/+}$ MEFs, we observed an increased ATP:ADP ratio at perinuclear positions, which gradually declined toward the periphery (Figure 2, A and B). By contrast, the ATP:ADP ratio decreased more rapidly at sites directly adjacent to perinuclear-restricted mitochondria in Miro1$^{-/-}$ MEFs,
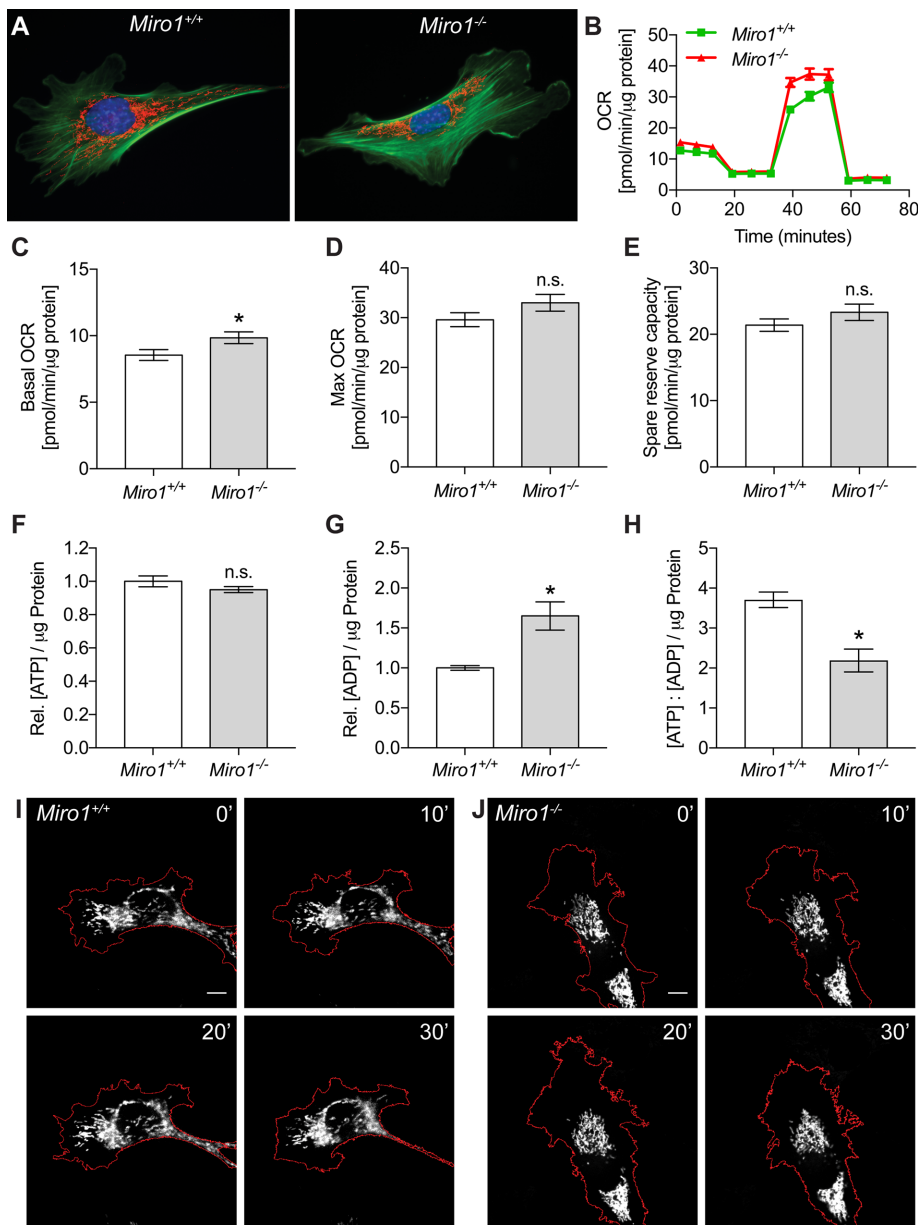
FIGURE 1: Miro1$^{-/-}$ MEFs have perinuclear-restricted mitochondria with intact mitochondrial metabolism. (A) Mitochondrial distribution in Miro1$^{+/+}$ and Miro1$^{-/-}$ MEFs. Green, actin; red, mitochondria; blue, nucleus. (B) OCR profiles of Miro1$^{+/+}$ (green) and Miro1$^{-/-}$ (red) MEFs. (C–E) Basal OCR (C), maximal OCR (D), and spare reserve capacity (E; maximal OCR − basal OCR) of Miro1$^{+/+}$ and Miro1$^{-/-}$ MEFs (*$p < 0.05$; n.s., not significant; Student's t test). (F, G) Relative ATP (F) and ADP (G) levels in Miro1$^{-/-}$ MEFs compared with Miro1$^{+/+}$ MEFs normalized to micrograms of protein (*$p < 0.05$; n.s., not significant; Student's t test). (H) Relative ATP:ADP ratio in Miro1$^{-/-}$ MEFs compared with Miro1$^{+/+}$ MEFs normalized to micrograms of protein (*$p < 0.05$, Student's t test). (I, J) Time-lapse images of mitochondrial movement in Miro1$^{+/+}$ (I) and Miro1$^{-/-}$ (J) MEFs. Cell outline is marked by a red line. (B–G) Data from one representative experiment (three replicates). Error bars show mean ± SE.

the complex I inhibitor rotenone reduced the total ATP:ADP ratio and dissipated intracellular energy gradients in Miro1$^{+/+}$ MEFs (Supplemental Figure S2, C–H), suggesting that mitochondria are the primary source of intracellular energy gradients in cultured MEFs.

We then analyzed the relationship between mitochondrial distribution and subcellular energy levels within the entire cell volume by LLSM. We first determined the 3D localization of mitochondrial networks in Miro1$^{+/+}$ and Miro1$^{-/-}$ MEFs transiently expressing mito-GFP and mCherry-LifeAct by LLSM (Figure 2, F and G, and Supplemental Figure S3). Independent of the cell height, which varied between 1 and 6 μm, mitochondria were positioned 0.5–1.5 μm from the ventral membrane in Miro1$^{+/+}$ and Miro1$^{-/-}$ MEFs (Figure 2, F and G, and Supplemental Figure S3). Thus Miro1 was not required for ventral positioning of mitochondria in MEFs. We then located the position of the highest ATP:ADP ratio along the z-axis throughout the entire cell volume by LLSM (Figure 2, D and E, Supplemental Figure S5, and Supplemental Movie S2). In Miro1$^{+/+}$ MEFs, the ATP:ADP ratio was highest at the ventral surface of the cell and decreased rapidly toward the dorsal membrane, independent of the volume of the cell (Figure 2, D and E, Supplemental Figure S5, and Supplemental Movie S2). We observed similar gradients along the z-axis in Miro1$^{-/-}$ MEFs; however, the gradient decreased more rapidly toward the dorsal membrane compared with controls (Supplemental Figure S5). Because mitochondrial distribution along the z-axis was not affected by Miro1 deletion (Figure 2G and Supplemental Figure S3), one interpretation of these results is that Miro1$^{-/-}$ MEFs consume more energy at perinuclear sites than Miro1$^{+/+}$ MEFs do. Finally, we observed the presence of ATP:ADP gradients in human-derived SUM159 breast cancer epithelial cells (Supplemental Figures S5 and S6), suggesting that observed intracellular 3D energy gradients are not specific to MEFs.

Miro1 deletion impairs membrane ruffling, leading-edge protrusion, and focal adhesion dynamics

During polarized cell migration, leading-edge protrusions extend the cell membrane in the direction of migration. This extension provides new sites for the formation of adhesive contacts between the cell and the substrate (Gardel et al., 2010; Huttenlocher and Horwitz, 2011). The biochemical processes underlying changes in membrane organization and cell adhesion at the leading edge consume considerable energy, which has recently been proposed to arise from mitochondrial sources (Cunniff et al., 2016). We thus tested whether altered mitochondrial localization and intracellular energy distribution in

correlating mitochondrial position with subcellular energy levels (Figure 2, A and B). Because PercevalHR is sensitive to intracellular pH levels (Berg et al., 2009), we confirmed that these results were not due to altered pH gradients in the cytoplasm (Supplemental Figure S2, A and B). Similar to biochemical data obtained using a luciferase-based assay (Figure 1, F–H), the mean ATP:ADP ratio measured by PercevalHR was lower in Miro1$^{-/-}$ than in Miro1$^{+/+}$ MEFs (Figure 2C). Finally, inhibition of the mitochondrial electron transport chain with
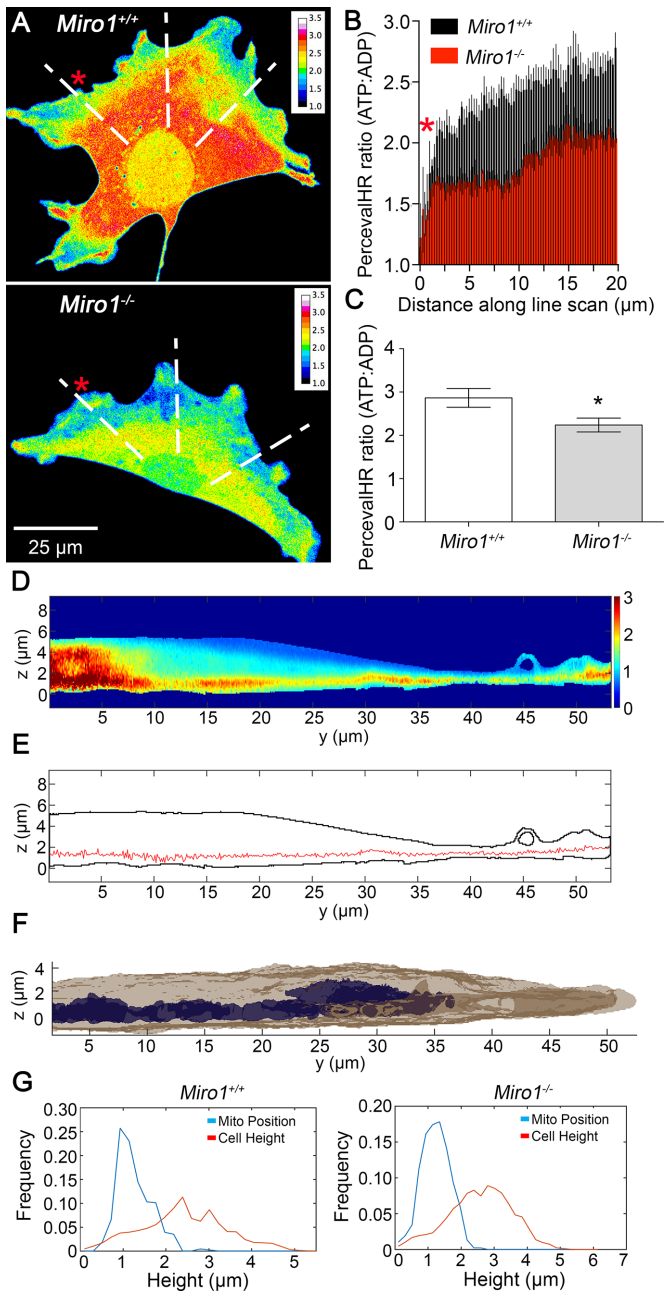
FIGURE 2: Energy distribution and mitochondrial positioning in MEFs. (A) Maximal intensity projections of ATP (λ_{ex} = 488 nm):ADP (λ_{ex} = 405 nm) ratiometric profiles of *Miro1*^{+/+} (top) and *Miro1*^{−/−} (bottom) MEFs expressing PercevalHR (λ_{em} = 540 nm). The entire cell volume was imaged in 500-nm optical sections by 3D spinning-disk confocal microscopy. White lines depict representative line scans used in B to determine spatial differences in ATP:ADP ratios. Red asterisks represent start of measurable signal at the cell edge in B. (B) Spatial plot of ATP:ADP ratios measured from the cell edge (0 μm, red asterisk) to the perinuclear region (20 μm) in *Miro1*^{+/+} and *Miro1*^{−/−} MEFs (five cells from one representative experiment, five line scans per cell represented in A as white lines). (C) Average whole-cell ATP:ADP ratio in *Miro1*^{+/+} and *Miro1*^{−/−} MEFs measured by PercevalHR fluorescence (five cells from one representative experiment; *p < 0.05, Student's t test). Error bars show mean ± SE. (D) Representative orthogonal (*yz*) view of ATP:ADP gradients in *Miro1*^{+/+} MEFs expressing PercevalHR and imaged by LLSM. Maximal intensity projection of 10 *yz*-optical sections (~1 μm thick). Orthogonal sections were taken from areas excluding the nucleus. (E) Tracing

Miro1^{−/−} MEFs impaired membrane reorganization events that support cell migration. Live-cell imaging of single cells showed decreased leading-edge protrusion in the direction of cell movement in *Miro1*^{−/−} compared with *Miro1*^{+/+} MEFs (Figure 3, A–C). The average number of membrane ruffles per frame, a hallmark of active cell migration (Deming *et al.*, 2008), was reduced from 17.6 ± 0.4 ruffles per frame in *Miro1*^{+/+} MEFs to 6.9 ± 0.3 ruffles per frame in *Miro1*^{−/−} MEFs (Figure 3, D and F). By contrast, analysis of membrane ruffle area showed no difference between genetic backgrounds (Figure 3, E and G). These combined results indicate that mitochondrial positioning at the leading edge supports energy-expensive actin-based membrane reorganization required for cell migration.

Focal adhesions (FAs) are dynamic protein assemblies forming and resolving on the basal surface of adherent cells. FAs form the physical connections between the actin cytoskeleton and the extracellular matrix and are essential for the propulsive force that contributes to the forward movement of cells (Zaidel-Bar *et al.*, 2004; Gardel *et al.*, 2010; Huttenlocher and Horwitz, 2011). Recent analyses in tumor cells (concurrent with this study) correlated mitochondrial positioning with FA dynamics (Caino *et al.*, 2015; Rivadeneira *et al.*, 2015). Both analyses suggested that mitochondrial positioning at the leading edge negatively affects FA size and stability, thereby increasing tumor cell migration and invasion. However, the global effects on metabolism and survival signaling pathways in cancer cells complicate interpretation of these results. Conversely, mitochondrial bioenergetics are not affected by deletion of *Miro1* (Figure 1; Nguyen *et al.*, 2014). We compared FA dynamics in *Miro1*^{+/+} and *Miro1*^{−/−} MEFs transiently expressing fluorescently tagged paxillin (Figure 4A), a marker for FAs (Deakin and Turner, 2008). Movies of growing and decaying FAs (Supplemental Movie S3) were analyzed using the FA Analysis Server (Berginski *et al.*, 2011; Berginski and Gomez, 2013) to quantify properties associated with FA assembly, stability, and disassembly. The average times for FA assembly (8 min) and disassembly (9 min) were comparable in both genotypes (Figure 4B). By contrast, the average time FAs resided in the stable phase was reduced in *Miro1*^{−/−} MEFs by ~50% relative to *Miro1*^{+/+} MEFs (Figure 4B). Analysis of the frequency distribution of individual FA lifetimes showed a significant decrease in *Miro1*^{−/−} MEFs compared with controls, with a time constant Tau of ~6 min for *Miro1*^{+/+} MEFs and ~3 min for *Miro1*^{−/−} MEFs (Figure 4C). FA growth and decay rates were also decreased in *Miro1*^{−/−} MEFs (Figure 4D), resulting in a decreased mean fluorescence intensity of stable-phase FAs compared with controls (Figure 4E). Such defects compromise the connection between the actin cytoskeleton and the extracellular matrix that is required for sufficient membrane pulling to actively move the cell forward. This is illustrated by the observation that *Miro1*^{−/−} MEFs form numerous small, short-lived membrane protrusions that fail to remain attached to the substrate (Supplemental Movie S1). Together these data indicate that depletion of metabolically active mitochondria from the leading edge and the reduced ATP:ADP ratio that results impair the assembly, stability, and disassembly phases of FAs.

(red line) of maximal intensity pixel ratio (λ_{em} = 540 nm) on excitation of PercevalHR at 488 nm (ATP) and 405 nm (ADP) throughout the entire volume of the cell (black outline). Note the consistent positioning of the highest ATP:ADP ratio along the ventral membrane. (F) Representative orthogonal view (*yz*) of a 3D rendering of mitochondria (blue) and the actin cytoskeleton (light brown) collected by LLSM to visualize ventral positioned mitochondrial networks. (G) Distribution of mitochondrial position (blue) and cell height (red) in *Miro1*^{+/+} (left) and *Miro1*^{−/−} (right) MEFs.
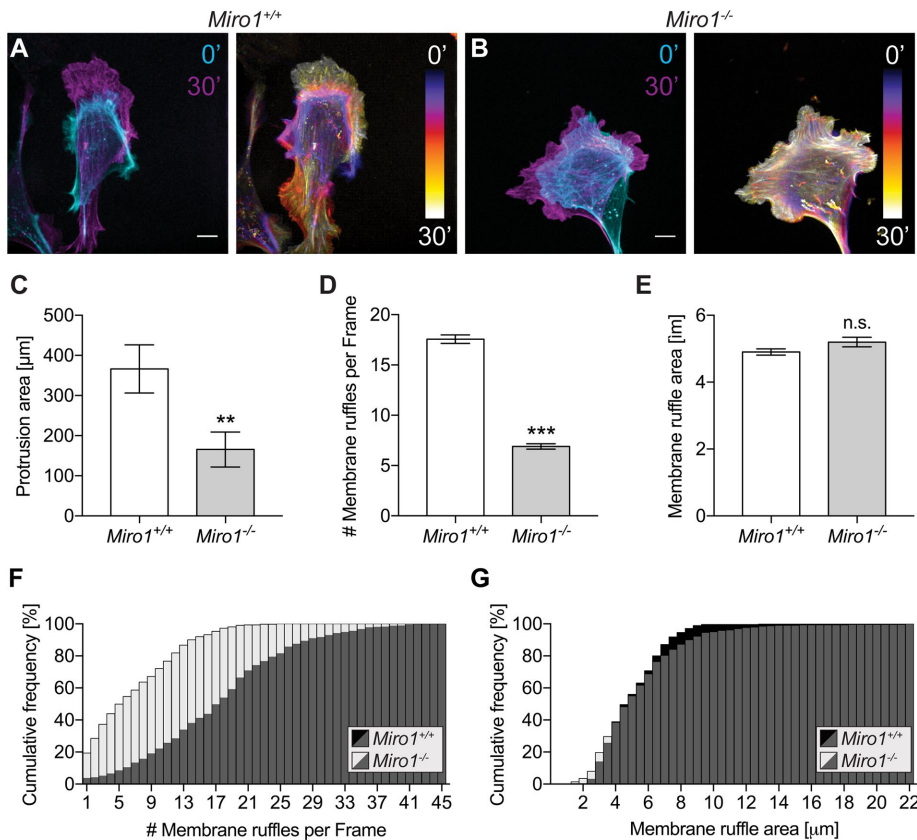
FIGURE 3: Leading-edge membrane dynamics of $Miro1^{+/+}$ and $Miro1^{-/-}$ MEFs. (A, B) Left, membrane position in $Miro1^{+/+}$ (A) and $Miro1^{-/-}$ (B) MEFs at 0 (cyan) and 30 (purple) min. Right, time-coded projection of membrane protrusion in $Miro1^{+/+}$ (A) and $Miro1^{-/-}$ (B) MEFs over 30 min. (C) Average membrane protrusion area in $Miro1^{+/+}$ and $Miro1^{-/-}$ MEFs (15 cells, ** $p < 0.01$, Student's t test). (D) Average number of membrane ruffles per frame in $Miro1^{+/+}$ and $Miro1^{-/-}$ MEFs (15 cells, *** $p < 0.001$, Student's t test). (E) Average membrane ruffle area in $Miro1^{+/+}$ and $Miro1^{-/-}$ MEFs (n.s., not significant; Student's t test). (F, G) Cumulative frequency of membrane ruffle events per image frame (F) and membrane ruffle area (G) in $Miro1^{+/+}$ and $Miro1^{-/-}$ MEFs. Bar, 10 µm (A, B). Data in C–E are from one representative experiment (three replicates). Error bars show mean ± SE.

Collective cell migration is compromised in $Miro1^{-/-}$ MEFs

$Miro1^{-/-}$ MEFs fail to form protruding membranes with extensive membrane ruffles and have disrupted FA dynamics. Such defects should affect the ability of $Miro1^{-/-}$ MEFs to collectively migrate over extended distances. To test this hypothesis, we plated $Miro1^{+/+}$ and $Miro1^{-/-}$ MEFs on either side of a specially designed tissue culture insert. Removal of the insert created a gap of ~450 ± 50 µm between the two confluent cell layers (Figure 5A). This system provides a more physiological setting in which to measure cell migration compared with traditional wound-healing assays, which can elicit aberrant responses due to cell damage (Van Horssen and ten Hagen, 2011). Quantification of gap closure showed that $Miro1^{+/+}$ MEFs were able to almost completely fill the gap within 8 h after insert removal (Figure 5, A and C, and Supplemental Movie S4). By contrast, closure by $Miro1^{-/-}$ MEFs was delayed, with transient reexpression of Myc-tagged Miro1 (Myc-Miro1) partially rescuing $Miro1^{-/-}$ MEF migration into the gap (Figure 5, A and C, and Supplemental Movie S4). Cotransfection of mito-GFP was used as an indicator of transfection efficiency (~75% of cells) and as a readout of mitochondrial redistribution due to exogenous Myc-Miro1 activity (Figure 5B and Supplemental Figure S7). Western blot analysis showed that the steady-state abundance of Myc-Miro1 expressed in $Miro1^{-/-}$ MEFs

was similar to that of endogenous Miro1 in $Miro1^{+/+}$ MEFs (Supplemental Figure S7). We also quantified the cell-front migration distances and velocities in these cell lines because the percentage of gap closure can be biased by initial gap size variation. The collective cell-front migration distance of $Miro1^{-/-}$ MEFs was reduced at all time points measured compared with controls (Figure 5D), translating into a decreased cell front velocity (21.5 ± 1.4 vs. 15.0 ± 1 µm/h; Figure 5E). Transient reexpression of Myc-Miro1 increased the cell-front migration distance and velocity of $Miro1^{-/-}$ MEFs (20 ± 0.9 µm/h; Figure5, D and E). Of importance, the presence of secreted factors from $Miro1^{+/+}$ MEFs was not sufficient to rescue migratory defects of $Miro1^{-/-}$ MEFs because cell-front migration distance of $Miro1^{-/-}$ MEFs was also decreased when $Miro1^{+/+}$ and $Miro1^{-/-}$ MEFs were plated in opposing insert sides (Figure 5F). These results establish that defects in parameters governing cell migration, such as membrane ruffling and FA dynamics, translate into decreased migratory speed in $Miro1^{-/-}$ MEFs.

Loss of $Miro1$ reduces cell velocity and migratory distance but not directionality of single-cell migration

Depending on the cell type, the extracellular matrix, and molecular patterning, cells migrate as a collective unit or as individual cells (Trepat *et al.*, 2012). Collective and single-cell migration modes retain similar migratory properties, the major difference being the presence of cell–cell junctions during collective migration, and serve overlapping and mutually exclusive purposes in the context of development and disease (Friedl and Wolf, 2003). To evaluate the role of mitochondrial distribution during single-cell migration, we analyzed the Euclidean and accumulated distances traveled, as well as velocity and directionality of individually migrating MEFs (Figure 6). $Miro1^{+/+}$, $Miro1^{-/-}$, and $Miro1^{-/-}$ MEFs transiently expressing Myc-Miro1 were plated at subconfluent density and imaged by live-cell fluorescence and differential interference contrast (DIC) microscopy for 6 h (Figure 6A). Individual cells were tracked by the locations of both their nucleus and cell body. Cells changing their direction of migration due to contact with other cells were excluded from the analysis. Quantification of accumulated and Euclidean distances traveled by each genetic background showed that $Miro1^{-/-}$ MEFs migrated shorter distances than $Miro1^{+/+}$ and Myc-Miro1–expressing $Miro1^{-/-}$ MEFs (Figure 6, B and C). Miro1 has been suggested to promote directional/persistent migration (Supplemental Figure S8, A and B; ratio of Euclidean over accumulated distance) of epithelial breast cancer cells by maintaining anterior positioned mitochondria (Desai *et al.*, 2013). Because both Euclidean and accumulated distances are similarly reduced in $Miro1^{-/-}$ MEFs, we found no significant difference in directionality of cell migration between the genetic backgrounds (Figure 6D). Quantification of the perinuclear mitochondrial network orientation relative to the direction of the leading edge revealed
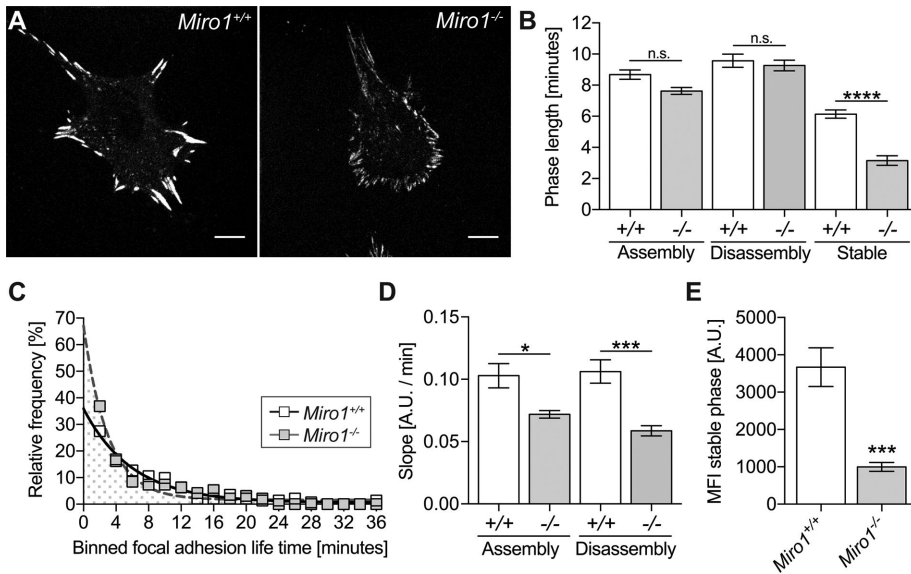
FIGURE 4: Focal adhesion dynamics are disrupted in Miro1$^{-/-}$ MEFs. (A) Still images from time-lapse microscopy movies of FAs in Miro1$^{+/+}$ and Miro1$^{-/-}$ MEFs transiently expressing mApple-paxillin. Bar, 10 µm. (B) Average FA assembly, disassembly. and stable phase lengths in Miro1$^{+/+}$ and Miro1$^{-/-}$ MEFs (15 cells; ***$p < 0.001$; one-way analysis of variance [ANOVA] with Tukey's post test). (C) Relative frequency of FA stable-phase lifetimes in Miro1$^{+/+}$ and Miro1$^{-/-}$ MEFs. Curves are fitted to binned data with a one-phase decay after exclusion of values <1. (D) Slope of fluorescence intensities derived from FA assembly and disassembly phases (eight cells; *$p < 0.033$, ***$p < 0.001$; one-way ANOVA with Tukey's posttest). (E) Mean fluorescence intensity (MFI) of stable-phase FAs in Miro1$^{+/+}$ and Miro1$^{-/-}$ MEFs (eight cells, ***$p < 0.001$; Student's t test). (B–E) Data from one representative experiment (three replicates). Error bars show mean ± SE.

that 63 ± 9% of Miro1$^{-/-}$ MEFs maintained anterior localized mitochondrial networks, compared with 90 ± 6% in Miro1$^{+/+}$ MEFs (Supplemental Figure S8C). Although this variance in anterior mitochondrial localization might explain the slight trend toward reduced directionality in Miro1$^{-/-}$ MEFs in some experiments, we believe that this is unlikely because the directionality difference was not statistically significant (Figure 6D). Furthermore, we found no difference in the forward migratory index (Supplemental Figure S8H), a readout of the capability of cells to maintain directionality during migration along chemotactic gradients, of Miro1$^{+/+}$ and Miro1$^{-/-}$ MEFs in a two-dimensional chemotaxis model system (Supplemental Figure S8, D–H). Finally, analysis of individual cell velocities revealed a reduction of cell migration speed in Miro1$^{-/-}$ cells (26.4 ± 1.4 vs. 21.0 ± 1.0 µm/h), whereas overexpression of Myc-Miro1 in Miro1$^{-/-}$ MEFs increased cell velocity over that of Miro1$^{+/+}$ MEFs (31.2 ± 1.2 µm/h; Figure 6E). These data strongly support a role for Miro1-mediated mitochondrial distribution in structural reorganization of the leading-edge membrane and focal adhesions during single-cell and collective migration.

Discussion

The reorganization of mitochondrial networks in large cells such as neurons has been extensively studied, and alterations in mitochondrial transport have been uncovered in numerous physiological and pathophysiological processes (Schwarz, 2013). By contrast, the requirement for mitochondrial positioning in smaller cells, such as fibroblasts or epithelial cells, is a new area of research in which active transport of mitochondria has only recently been implicated in immune function (Campello et al., 2006; Quintana and Hoth, 2012; Morlino et al., 2014), response to cell stress (Al-Mehdi et al., 2012;

Liesa and Shirihai, 2013; Hoppins, 2014), and cell migration (Wang et al., 2011; Desai et al., 2013; Zhao et al., 2013; Caino et al., 2015; Rivadeneira et al., 2015; Cunniff et al., 2016). Unlike neurons, which can span up to 1 m in length, epithelial cells and fibroblasts are much smaller (25–75 µm), and a requirement for mitochondrial positioning to meet local energy demands has appeared to be less obvious but not without speculation (Jayashankar and Rafelski, 2014). In support of this idea, enzymes localized at sites distant from energy sources are more sensitive to lower levels of ATP, an example of the microheterogeneity of ATP supply independent of subcellular compartmentalization (Jones, 1986). In addition, using purified mitochondria and Xenopus egg extracts, Niethammer et al. (2008) visualized energy gradients extending 20–50 µm from ATPase-coupled beads in vitro. Recent biochemical measurements also documented different ATP:ADP ratios in pseudopods versus cell bodies of migrating tumor cells (Cunniff et al., 2016). However, direct visual evidence for the existence of such energy gradients in vivo was lacking (Jayashankar and Rafelski, 2014) before our present results.

By taking advantage of LLSM, we now present the first instance of full 3D imaging of ATP:ADP ratios throughout the entire volume of the cell and demonstrate the existence of intracellular energy gradients emanating from mitochondria. In agreement with our data, previous analysis of imaging data obtained with the ATP:ADP fluorescent sensor PercevalHR by single-plane confocal microscopy indicated a uniform ATP:ADP ratio throughout the entire bottom of cells attached to a support (Berg et al., 2009; Tantama et al., 2013). The highest ratio of ATP:ADP is found at the position of dense mitochondrial networks around the nucleus and gradually declines as mitochondrial density decreases at more peripheral sites. We show that the positioning of mitochondria within 1 µm of the ventral membrane correlates with an increased ATP:ADP ratio, which decreases toward the dorsal surface, where mitochondrial density is lowest. Because we would not expect PercevalHR to enter the mitochondrial matrix without a mitochondrial targeting sequence (Chacinska et al., 2009), we are most likely visualizing newly synthesized ATP close to the surface of mitochondria. Miro1$^{-/-}$ MEFs, which fail to redistribute their mitochondrial networks away from perinuclear sites, show an exaggerated decrease in the ATP:ADP ratio at peripheral sites devoid of mitochondria, providing additional direct evidence that mitochondrial positioning shapes intracellular energy gradients. From these observations, we conclude that mitochondrial distribution shapes intracellular energy gradients in nonneuronal cultured cells. These gradients are presumably a consequence of local imbalances between ATP production by mitochondria and its consumption by energy-expensive processes at distant sites. More generally, our findings substantiate a justification to investigate the possibility that mitochondrial positioning might also meet the localized demand for reactive oxygen species signaling and calcium buffering (McBride et al., 2006; Osellame et al., 2012).

To date, all studies concerning the positioning of mitochondria during cell migration have been carried out in cancer cell lines
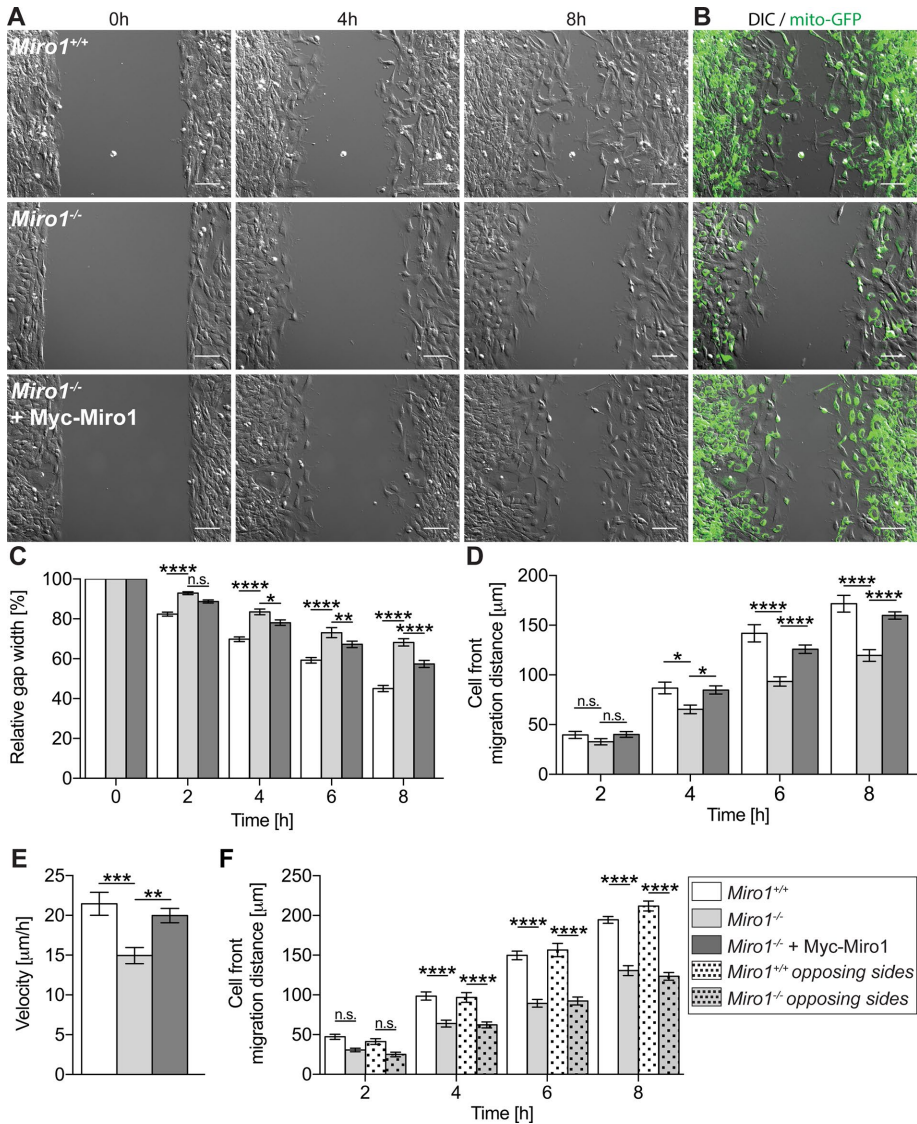
FIGURE 5: *Miro1* deficiency impairs collective cell migration. (A) Representative DIC images of gap closure by *Miro1^{+/+}^*, *Miro1^{−/−}^*, and *Miro1^{−/−}^* MEFs transiently expressing Myc-Miro1 at indicated times after insert removal. (B) Cotransfection of mito-GFP was used to determine transfection and rescue efficiency. (C, D) Relative gap width (C) and cell-front migration distance (D) over time (n.s., not significant; *p < 0.033, **p < 0.002, ****p < 0.0001; two-way ANOVA with Tukey's posttest). (E) Average cell-front velocity of migrating MEFs (**p < 0.002, ***p < 0.0002; one-way ANOVA with Tukey's posttest). (F) Comparison of cell-front migration distances of *Miro1^{+/+}^* and *Miro1^{−/−}^* MEFs. Textured bars (mixed culture) show data from *Miro1^{+/+}^* and *Miro1^{−/−}^* MEFs plated into opposing insert sides (****p < 0.0001, two-way ANOVA with Tukey's post test). Bar, 100 μm (A, B). For C–F, data are from one representative experiment (three replicates). Error bars show mean ± SE.

cytoskeleton and the extracellular matrix. Our data contrast with recent analysis in epithelial cancer cells, which concluded that depletion of mitochondria from the cell periphery increases FA stability (Caino et al., 2015; Rivadeneira et al., 2015). Cell type–specific modes of migration (epithelial vs. fibroblast), epithelial-to-mesenchymal transition–induced alterations to migration (Wong et al., 2014), or altered metabolic programming associated with tumorigenesis (Hanahan and Weinberg, 2011) may explain these differences. Consequently *Miro1^{−/−}^* MEFs migrated more slowly than *Miro1^{+/+}^* MEFs in the context of collective and single-cell migration. Of importance, reexpression of Myc-Miro1 redistributed the mitochondrial network to the cell periphery and restored cell migration of *Miro1^{−/−}^* MEFs to wild-type levels. These findings provide a direct demonstration that precise subcellular positioning of functioning mitochondria is crucial for subcellular events controlling cell migration.

Our results raise questions regarding the role of mitochondrial distribution during development, when cell migration is absolutely essential (Trepat et al., 2012). Germline inactivation of *Miro1* in mice leads to apparently normal gross development, with postnatal death from unexpanded lungs due to specific defects in motor neuron development required for breathing (Nguyen et al., 2014). Loss of *Miro1* or the *Miro1* paralogue *Miro2* has not been studied in the context of development in mammalian cells. Furthermore, little is known about the expression patterns of *Miro1* and *Miro2* during development compared with a mature organism. Although it is possible that *Miro1* is dispensable for normal development in tissues other than the CNS, this would be surprising because defective mitochondrial positioning causes migratory defects in multiple cell types (Campello et al., 2006; Wang et al., 2011; Desai et al., 2013; Zhao et al., 2013; Caino et al., 2015; Rivadeneira et al., 2015; Cunniff et al., 2016; this study). A detailed analysis of individual organs, tissues, and cell types in *Miro1^{−/−}^* mice may reveal more subtle defects

associated with *Miro1* loss. In addition, further studies are needed to decipher the function and regulation of other protein assemblies (including the *Miro1* paralogue *Miro2*) that guide mitochondrial movement in different cell types and tissues during development.

In conclusion, we took advantage of the improved spatial resolution attained by newly implemented 3D fluorescence LLSM to demonstrate directly the existence of subcellular ATP:ADP gradients in living mammalian cells. We then showed that the intracellular energy gradients originate from the location of highest mitochondrial abundance. Finally, we showed that Miro1-mediated distribution of the mitochondrial network toward the cell periphery containing the cortical cytoskeleton helps promote cell migration in part by supporting

(Wang et al., 2011; Desai et al., 2013; Zhao et al., 2013; Caino et al., 2015; Rivadeneira et al., 2015; Cunniff et al., 2016). Given that tumorigenic properties such as increased growth factor signaling, metabolic alterations, and changes in metabolite levels influence cell migration (Han et al., 2013), we believe that our results using *Miro1^{−/−}^* MEFs, which largely retain normal mitochondrial function, establish a baseline for positioning of metabolically intact mitochondria during non–tumor-associated cell migration. Cells completely lacking *Miro1* fail to form extensive lamellipodia and membrane ruffles, a readout of active cell migration. Furthermore, the rates of FA growth and decay, as well as FA stability, are altered by *Miro1* deletion, compromising the connection between the actin
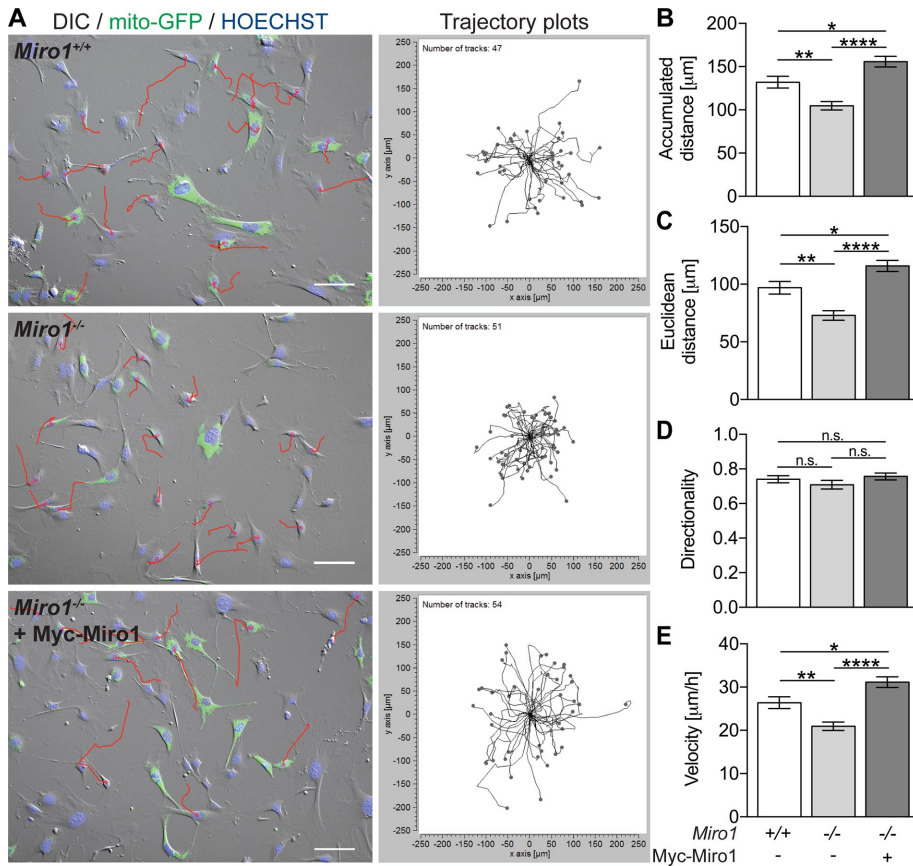
FIGURE 6: Miro1-mediated mitochondrial positioning accelerates single-cell migration. (A) Left, representative images and traces of randomly migrating *Miro1⁺/⁺*, *Miro1⁻/⁻*, and *Miro1⁻/⁻* MEFs transiently expressing Myc-Miro1. Cotransfection of mito-GFP was used to determine transfection and rescue efficiency. Hoechst stain was used to label nuclei. Bar, 100 μm. Right, representative trajectory plots of *Miro1⁺/⁺*, *Miro1⁻/⁻* =, and *Miro1⁻/⁻* MEFs transiently expressing Myc-Miro1. Each track originates at coordinates (0, 0) and ends at a dot. (B, C) Accumulated (B) and Euclidean (C) distances migrated by *Miro1⁺/⁺*, *Miro1⁻/⁻*, and *Miro1⁻/⁻* MEFs transiently expressing Myc-Miro1 (n.s, not significant; *$p < 0.033$, **$p < 0.002$, ****$p < 0.0001$; one-way ANOVA with Tukey's posttest). (D, E) Velocity (D) and directionality (E) of randomly migrating *Miro1⁺/⁺*, *Miro1⁻/⁻*, and *Miro1⁻/⁻* MEFs transiently expressing Myc-Miro1 (n.s., not significant; *$p < 0.033$, **$p < 0.002$, ****$p < 0.0001$; one-way ANOVA with Tukey's posttest). For B–E, data are from one representative experiment (three replicates). Error bars show mean ± SE.

membrane protrusion and FA dynamics. These findings provide a direct demonstration that precise positioning of functional mitochondria is crucial for subcellular events such as control of cell migration.

MATERIALS AND METHODS

Cell culture
Generation of *Miro1⁻/⁻* mice has been described (Nguyen *et al.*, 2014). MEFs were isolated from *Miro1⁻/⁻* and control littermates at embryonic gestation day 13 and immortalized by lentiviral transduction with simian virus 40 large T antigen (Zhu *et al.*, 1991; Nguyen *et al.*, 2014). MEFs were cultured in high-glucose DMEM (Invitrogen) supplemented with 10% (vol/vol) fetal bovine serum (FBS; Atlanta Biologicals), 2 mM ʟ-glutamine (Invitrogen), 100 U/ml penicillin/streptomycin (Invitrogen), and 50 mM β-mercaptoethanol (Sigma-Aldrich). Human-derived, mostly diploid SUM159 cells were grown in DMEM/F-12/GlutaMAX (Invitrogen) supplemented with 5% FBS (Atlanta Biologicals), 100 U/ml penicillin and streptomycin (VWR International), 1 μg/ml hydrocortisone (Sigma-Aldrich), 5 μg/ml insulin (Sigma-Aldrich), and 10 mM 4-(2-hydroxyethyl)-1-piperazineethanesulfonic acid (HEPES; Mediatech), pH 7.4.

Plasmids and transfections
Myc-tagged Miro1 isoform 1 was described previously (Nguyen *et al.*, 2014). Mitochondrial-targeted GFP (632432) was purchased from Clontech. mApple-paxillin (Smith *et al.*, 2013) was a gift from M. Beckerle (University of Utah). The mCherry-LifeAct (54491) and PercevalHR (49082) plasmids were purchased from Addgene. Plasmids were purified by CsCl gradient. MEFs were grown to 75% confluency and transfected with the indicated plasmids (1 μg of each plasmid per 100,000 cells) using the Neon electroporation system (Invitrogen; 10-μl kit, one pulse, 1300 mV, 30 ms) according to manufacturer's description. Cells were grown in MEF medium without penicillin/streptomycin for 24 h posttransfection. SUM159 cells were transfected with PercevalHR using TransfeX (American Type Culture Collection) in complete medium. Cells were imaged 24–48 h posttransfection.

Live-cell imaging of actin and focal adhesion dynamics
Glass coverslips (25 mm, #1.5; Warner Instruments, Hamden, CT) were sonicated for 15 min in 100% ethanol and dried. At 24 h posttransfection, cells were plated onto coverslips and allowed to adhere overnight in complete medium. For imaging of mitochondrial movement, leading-edge membrane, and focal adhesion dynamics, the coverslips were placed in a temperature-controlled humidified chamber (20/20 Technology, Wilmington, NC) in FluoroBrite (ThermoScientific) imaging medium supplemented with 5% FBS and 10 mM HEPES and mounted on the piezoelectric-driven stage of a Mariana imaging system (Intelligent Imaging Innovations, Denver, CO) based on an Axiovert 200M inverted microscope (Carl Zeiss, Thornwood, NY), a CSU-X1 spinning-disk confocal unit (Yokogawa Electric Corporation, Tokyo, Japan), and a 63× objective (Plan Apochromat, numerical aperture [NA] 1.4; Carl Zeiss). Images were acquired at 1-min intervals for 30–60 min.

Measurement of ATP and ADP levels
ATP and ADP levels in *Miro1⁺/⁺* and *Miro1⁻/⁻* MEFs were determined using an ADP:ATP ratio kit (ab65313; Abcam) according to manufacturer's descriptions. Briefly, 35,000 cells per genotype were seeded into 24-well dishes and allowed to adhere overnight at 37°C and 5% CO_2. The next day, cells were washed with phosphate-buffered saline (PBS) and lysed in 180 μl of cold nucleotide release buffer for 10 min on ice. Lysates were transferred to Eppendorf tubes, and cell debris was removed by centrifugation at $14,000 \times g$ for 10 min at 4°C. To measure ATP levels, 50 μl of cell lysate was added to 100 μl of reaction mix in 96-well plates, and luminescence was measured using a Veritas Microplate Luminometer (Turner BioSystems). Subsequently 10 μl of ADP-converting enzyme was added to each well, and luminescence was measured again. ADP levels were calculated by subtracting luminescence values of the first measurement from

the luminescence values obtained on conversion of all ADP to ATP. In each experiment, all measurements were performed in triplicate. Luminescence values are shown as relative data normalized to values from Miro1$^{+/+}$ MEFs and to micrograms of protein determined by bicinchoninic acid protein assay (BCA) assay (Pierce) according to manufacturer's descriptions.

Seahorse extracellular flux analysis

To analyze mitochondrial bioenergetics in Miro1$^{+/+}$ and Miro1$^{-/-}$ MEFs, 15,000 cells of each genotype were plated into Seahorse XF96 Cell Culture Microplates (Agilent), centrifuged at 200 × g for 5 min, and allowed to adhere for 6 h in MEF medium at 37°C and 5% CO_2. Subsequently the cells were washed with XF base medium (Agilent) supplemented with 1 mM sodium pyruvate, 2 mM L-glutamine, and 25 mM glucose and adjusted to pH 7.4, and mitochondrial OCRs were determined using the Seahorse XF Cell Mito Stress Test Kit (Agilent) and a Seahorse XF96 Analyzer (Agilent) according to manufacturer's description. Basal OCRs were measured in XF base medium (Agilent) supplemented with 1 mM sodium pyruvate, 2 mM L-glutamine, and 25 mM glucose and adjusted to pH 7.4. Oxygen consumption due to mitochondrial ATP production was determined after injection of oligomycin to a final concentration of 1 μg/ml to inhibit mitochondrial ATP-synthase function. Maximal OCR was measured after injection of carbonilcyanide p-triflouromethoxyphenylhydrazone (FCCP) to a final concentration of 0.5 μM to uncouple the mitochondrial respiratory chain. Nonmitochondrial oxygen consumption was measured after injection of rotenone and antimycin A to a final concentration of 0.5 μM to inhibit respiratory chain complexes I and III, respectively. For each condition, oxygen consumption was measured at three time points, each consisting of 3 min of mixing followed by 3 min of measurement. OCR values from 16–24 wells per genotype were normalized to micrograms of protein per well determined by BCA assay (Pierce) according to manufacturer's descriptions. Basal and maximal OCRs were calculated by subtracting the lowest value measured after addition of rotenone/antimycin A from the last value measured before addition of oligomycin or the highest value measured upon addition of FCCP, respectively. The spare respiratory capacity was calculated by subtracting the basal OCR values from the maximal OCR values. All experiments were performed with the help of the University of Utah Metabolic Phenotyping Core Facility.

Live-cell imaging of PercevalHR by spinning-disk confocal microscopy

Imaging of PercevalHR by spinning-disk confocal microscopy was carried out under the same conditions as described. Cells expressing PercevalHR were sequentially excited using 405- and 488-nm lasers with emission collected at 540 nm for both channels as described in the original publication of the probe (Berg et al., 2009). Z-stacks were collected for the entire volume of the cell in 500-nm optical sections. Images were background subtracted before calculating the pixel-by-pixel ratio of the 488:405 (ATP bound/ADP bound) signals. Mean ATP:ADP ratios of individual cells were calculated from maximum intensity projections using the ImageJ measurement tool. Line scans were used to determine spatial changes in PercevalHR signal from the leading edge to perinuclear positions. For rotenone experiments, identical cells were imaged before and after addition of 10 μM rotenone (diluted in imaging medium) to the imaging chamber.

LLSM imaging of PercevalHR, mitochondria, and actin

MEFs and SUM159 cells expressing PercevalHR or MEFs expressing mito-GFP and mCherry-LifeAct were plated onto 5-mm coverslips

and imaged ~24 h later in FluoroBrite DMEM medium (ThermoFisher Scientific) supplemented with 5% FBS and 20 mM HEPES, pH 7.4. Imaging of SUM159 and Miro1$^{+/+}$ and Miro1$^{-/-}$ MEFs was carried out using LLSM in the Kirchhausen lab (Aguet et al., 2016) using a square lattice configuration in dithered mode (Chen et al., 2014). PercevalHR, mito-GFP, and mCherry-LifeAct were excited with the light sheet generated using an excitation inner/outer aperture of 0.35/0.4. Because the recorded images of optical sections of the cells exceeded the nondiffracting region of the lattice light sheet, images were cropped to the nondiffracting region of the light sheet for analysis.

For MEFs expressing PercevalHR, images were recorded using a Hamamatsu ORCA-Flash4.0 scientific complementary metal-oxide semiconductor (sCMOS) camera, where each plane of the imaged volume was sequentially excited using 405- and 488-nm lasers (~27 and ~70 μW at the back aperture of the excitation objective, respectively) and exposed for 497 ms. Cells were imaged by stepping the sample stage at 400-nm intervals, which corresponded to 209-nm steps in the z-axis, thereby capturing a pre-deskewed volume of ~80 × 53 × 75 μm^3 (768 × 512 × 150 pixels).

For SUM159 cells expressing PercevalHR, images were recorded using a Hamamatsu ORCA-Flash4.0 sCMOS camera, where each plane of the imaged volume was sequentially excited using 405- and 488 nm lasers (~24 and ~35 μW at the back aperture of the excitation objective, respectively) and exposed for 497 and 47 ms, respectively. Cells were imaged by stepping the sample stage at 500-nm intervals, which corresponded to 261-nm steps in the z-axis, thereby capturing a pre-deskewed volume of ~106 × 53 × 75 μm^3 (1024 × 512 × 150 pixels).

For MEFs expressing mito-GFP and mCherry-LifeAct, images were recorded using a dual Andor iXon 897 Ultra electron-multiplying charge-coupled device (EMCCD) camera setup, where each plane of the imaged volume was sequentially excited using 488- and 560 nm lasers (~3.8 and ~190 μW at the back aperture of the excitation objective, respectively) and exposed for 19.8 ms. The emission was spectrally separated and recorded on the two EMCCD cameras using a dichroic (Semrock FF560 FDi01 25 × 36). Cells were imaged by moving the sample stage at 500-nm step sizes, corresponding to 261-nm intervals in the z-axis, thereby capturing a pre-deskewed volume of ~53 × 42 × 50 μm^3 (512 × 400 × 99 pixels).

Analysis of 3D positioning of mitochondria

LLSM images of Miro1$^{+/+}$ and Miro1$^{-/-}$ MEFs were segmented using the mCherry-LifeAct signal (see Supplemental Figure S3 for analysis workflow). The deskewed images were 1) preprocessed using a Gaussian filter to remove high-frequency noise, 2) resampled to make x-, y-, and z-voxels isotropic, and 3) segmented by using an Otsu thresholding method. To segment the mitochondria, the same protocol was applied, preceded by a top-hat filter (Koopman et al., 2006; Iannetti et al., 2016). To position the mitochondria in the 3D space, we skeletonized the segmented structures and measured the distance of the skeleton coordinates from the bottom surface of the cell (i.e., the membrane–coverslip interface; Nikolaisen et al., 2014). In Figure 2 and Supplemental Figure S2, the distribution of these distances is compared with the thickness distribution of the same cell.

Mapping ATP:ADP ratio using PercevalHR and LLSM

The images acquired for PercevalHR were deskewed and resampled to make x-, y-, and z-voxels isotropic. After flat-field correction and normalization, the ratio of the background-subtracted fluorescent signals (emission, 540 nm) from the two emissions (excited respectively at 488 and 405 nm) was computed. We considered only regions with a signal-to-noise ratio for both emissions >3 to ensure

that sufficient signal was collected for analysis. The average signal across 10 planes along the z-axis is reported in Figure 2 and Supplemental S4. We estimated the outline of the cell by performing an Otsu thresholding method, as well as the maximum intensity pixel in the z-direction. The median of the intensity distribution at indicated distances from the bottom surface ((i.e., the membrane–coverslip interface) is plotted as a red line along a mask of the cell outline.

Cell migration assays

For analysis of collective cell migration, cells were plated 12 h posttransfection in specially designed tissue culture inserts (ibidi, Martinsried, Germany) placed in a multiwell glass-bottom dish (CellVis). Inserts were removed after cells reached confluency (12–24 h), and gap closure was imaged at three image fields per genotype by DIC and fluorescence microscopy every 10 min for 12 h in normal MEF medium using a temperature-controlled, 5% CO_2, humidified chamber (Pathology Devices). Samples were illuminated with a Sutter TLED+ lamp, and time-lapse movies were collected with wide-field illumination with a Nikon Eclipse Ti, 10× objective (Plan Apochromat, NA 0.45) with an Andor Clara interline CCD camera. To determine the relative gap closure and migration distance over time, the gap width and migration distance were measured along eight horizontal lines in each image field at the indicated times. The average velocity was calculated by dividing the migrated distance between 0 and 8 h by the time interval.

For analysis of single-cell migration, MEFs were plated to subconfluent density in a multiwell glass-bottom dish (CellVis) 12 h posttransfection and allowed to adhere for 12–24 h. Before imaging, 10 ng/ml Hoechst (Invitrogen) was added to the medium, and random migration was imaged from 5–10 image fields every 10 min for 6 h by DIC and fluorescence microscopy as described. Randomly migrating cells that displaced the nucleus and the cell body and did not change their direction of migration due to interaction with other cells were manually tracked using the MTrack ImageJ macro. The accumulated and Euclidean distances, as well as average cell velocity and directionality, were calculated using the ibidi Chemotaxis and Migration Tool 2.0.

Focal adhesion analysis

Miro1$^{+/+}$ and *Miro1$^{-/-}$* MEFs were transiently transfected with mApple-paxillin by electroporation. The next day, the cells were replated onto precleaned glass coverslips and allowed to attach overnight. The bottom surface of mApple-paxillin–expressing cells was imaged by spinning-disk confocal microscopy every minute (excitation at 561 nm for 100-ms exposure) for 30–60 min. Focal adhesion parameters, including assembly, stability, disassembly, growth rate, and stable-phase mean fluorescence intensity, were determined for each cell movie submitted to the Focal Adhesion Analysis Server (FAAS; Berginski *et al.*, 2011; Berginski and Gomez, 2013). Individual focal adhesions from each genetic background were also analyzed by hand to ensure that the FAAS analysis contained representative findings. To determine the time constant Tau, the distribution of all stable-phase lifetimes was fitted to binned data (bin size, 2 min) after exclusion of all values <1 using a one-phase decay model in GraphPad Prism 7.

Membrane ruffling and membrane displacement

Miro1$^{+/+}$ and *Miro1$^{-/-}$* MEFs transiently expressing mCherry-LifeAct and mito-GFP were plated onto precleaned glass coverslips and imaged by spinning-disk confocal microscopy (100-ms exposure time for 488- and 561-nm excitation) every minute for 30–60 min. The area of membrane protrusion was determined by measuring membrane area displaced in the direction of cell migration by comparing the first

and last frames of live-cell imaging movies using ImageJ. Membrane ruffling was determined using the ImageJ RuffleQuant macro in ImageJ as previously described (Deming *et al.*, 2008).

Statistics

All experiments were performed in biological triplicates using three independently isolated and immortalized MEF lines for each genotype. Figures show representative data from one experiment in one cell line. Where applicable, the number of quantified cells per experiment is indicated. *p* values were calculated in GraphPad Prism 7 using the indicated statistical test.

REFERENCES

Aguet F, Upadhyayula S, Gaudin R, Chou YY, Cocucci E, He K, Chen BC, Mosaliganti K, Pasham M, Skillern W, *et al.* (2016). Membrane dynamics of dividing cells imaged by lattice light-sheet microscopy. Mol Biol Cell 27, 3418–3435.

Al-Mehdi A-B, Pastukh VM, Swiger BM, Reed DJ, Patel MR, Bardwell GC, Pastukh VV, Alexeyev MF, Gillespie MN (2012). Perinuclear mitochondrial clustering creates an oxidant-rich nuclear domain required for hypoxia-induced transcription. Sci Signal 5, ra47.

Berg J, Hung YP, Yellen G (2009). A genetically encoded fluorescent reporter of ATP:ADP ratio. Nat Methods 6, 161–166.

Berg JM, Tymoczko JL, Stryer L (2002). The Regulation of Cellular Respiration Is Governed Primarily by the Need for ATP, New York: W. H. Freeman.

Berginski ME, Gomez SM (2013). The Focal Adhesion Analysis Server: a web tool for analyzing focal adhesion dynamics. F1000Research 2, 68.

Berginski ME, Vitriol EA, Hahn KM, Gomez SM (2011). High-resolution quantification of focal adhesion spatiotemporal dynamics in living cells. PLoS One 6, e22025.

Brickley K, Smith MJ, Beck M, Stephenson FA (2005). GRIF-1 and OIP106, members of a novel gene family of coiled-coil domain proteins: association in vivo and in vitro with kinesin. J Biol Chem 280, 14723–14732.

Cai Q, Davis ML, Sheng Z-H (2011). Regulation of axonal mitochondrial transport and its impact on synaptic transmission. Neurosci Res 70, 9–15.

Cai Q, Sheng Z-H (2009). Mitochondrial transport and docking in axons. Exp Neurol 218, 257–267.

Caino MC, Ghosh JC, Chae YC, Vaira V, Rivadeneira DB, Faversani A, Rampini P, Kossenkov AV, Aird KM, Zhang R, *et al.* (2015). PI3K therapy reprograms mitochondrial trafficking to fuel tumor cell invasion. Proc Natl Acad Sci USA 112, 8638–8643.

Campello S, Lacalle RA, Bettella M, Mañes S, Scorrano L, Viola A (2006). Orchestration of lymphocyte chemotaxis by mitochondrial dynamics. J Exp Med 203, 2879–2886.

Chacinska A, Koehler CM, Milenkovic D, Lithgow T, Pfanner N (2009). Importing mitochondrial proteins: machineries and mechanisms. Cell 138, 628–644.

Chen BC, Legant WR, Wang K, Shao L, Milkie DE, Davidson MW, Janetopoulos C, Wu XS, Hammer JA 3rd, Liu Z, *et al.* (2014). Lattice

light-sheet microscopy: imaging molecules to embryos at high spatio-temporal resolution. Science 346, 1257998.

Cunniff B, McKenzie AJ, Heintz NH, Howe AK (2016). AMPK activity regulates trafficking of mitochondria to the leading edge during cell migration and matrix invasion. Mol Biol Cell 27, 2662–2674.

Deakin NO, Turner CE (2008). Paxillin comes of age. J Cell Sci 121, 2435–2444.

Deming PB, Campbell SL, Baldor LC, Howe AK (2008). Protein kinase a regulates 3-phosphatidylinositide dynamics during platelet-derived growth factor-induced membrane ruffling and chemotaxis. J Biol Chem 283, 35199–35211.

Desai SP, Bhatia SN, Toner M, Irimia D (2013). Mitochondrial localization and the persistent migration of epithelial cancer cells. Biophys J 104, 2077–2088.

Divakaruni AS, Paradyse A, Ferrick DA, Murphy AN, Jastroch M (2014). Analysis and interpretation of microplate-based oxygen consumption and pH data. Methods Enzymol 547, 309–354.

Fransson Å, Ruusala A, Aspenström P (2003). Atypical Rho GTPases have roles in mitochondrial homeostasis and apoptosis. J Biol Chem 278, 6495–6502.

Fransson Å, Ruusala A, Aspenström P (2006). The atypical Rho GTPases Miro-1 and Miro-2 have essential roles in mitochondrial trafficking. Biochem Biophys Res Commun 344, 500–510.

Frederick RL, McCaffery JM, Cunningham KW, Okamoto K, Shaw JM (2004). Yeast Miro GTPase, Gem1p, regulates mitochondrial morphology via a novel pathway. J Cell Biol 167, 87–98.

Friedl P, Wolf K (2003). Tumour-cell invasion and migration: diversity and escape mechanisms. Nat Rev Cancer 3, 362–374.

Gardel ML, Schneider IC, Aratyn-Schaus Y, Waterman CM (2010). Mechanical integration of actin and adhesion dynamics in cell migration. Annu Rev Cell Dev Biol 26, 315–333.

Glater EE, Megeath LJ, Stowers RS, Schwarz TL (2006). Axonal transport of mitochondria requires milton to recruit kinesin heavy chain and is light chain independent. J Cell Biol 173, 545–557.

Guo X, Macleod GT, Wellington A, Hu F, Panchumarthi S, Schoenfield M, Marin L, Charlton MP, Atwood HL, Zinsmaier KE (2005). The GTPase dMiro is required for axonal transport of mitochondria to Drosophila synapses. Neuron 47, 379–393.

Han T, Kang D, Ji D, Wang X, Zhan W, Fu M, Xin H-B, Wang J-B (2013). How does cancer cell metabolism affect tumor migration and invasion? Cell Adhes Migr 7, 395–403.

Hanahan D, Weinberg RA (2011). Hallmarks of cancer: the next generation. Cell 144, 646–674.

Hollenbeck PJ, Saxton WM (2005). The axonal transport of mitochondria. J Cell Sci 118, 5411–5419.

Hoppins S (2014). The regulation of mitochondrial dynamics. Curr Opin Cell Biol 29, 46–52.

Huttenlocher A, Horwitz AR (2011). Integrins in cell migration. Cold Spring Harb Perspect Biol 3, a005074.

Iannetti EF, Smeitink JAM, Beyrath J, Willems PHGM, Koopman WJH (2016). Multiplexed high-content analysis of mitochondrial morphofunction using live-cell microscopy. Nat Protoc 11, 1693–1710.

Jayashankar V, Rafelski SM (2014). Integrating mitochondrial organization and dynamics with cellular architecture. Curr Opin Cell Biol 26, 34–40.

Jones DP (1986). Intracellular diffusion gradients of O2 and ATP. Am J Physiol 250, C663–C675.

Klosowiak JL, Focia PJ, Chakravarthy S, Landahl EC, Freymann DM, Rice SE (2013). Structural coupling of the EF hand and C-terminal GTPase domains in the mitochondrial protein Miro. EMBO Rep 14, 968–974.

Klosowiak JL, Park S, Smith KP, French ME, Focia PJ, Freymann DM, Rice SE (2016). Structural insights into Parkin substrate lysine targeting from minimal Miro substrates. Sci Rep 6, 33019.

Koopman WJH, Visch H-J, Smeitink JAM, Willems PHGM (2006). Simultaneous quantitative measurement and automated analysis of mitochondrial morphology, mass, potential, and motility in living human skin fibroblasts. Cytometry A 69, 1–12.

Liesa M, Shirihai OS (2013). Mitochondrial dynamics in the regulation of nutrient utilization and energy expenditure. Cell Metab 17, 491–506.

MacAskill AF, Rinholm JE, Twelvetrees AE, Arancibia-Carcamo IL, Muir J, Fransson A, Aspenstrom P, Attwell D, Kittler JT (2009). Miro1 is a calcium sensor for glutamate receptor-dependent localization of mitochondria at synapses. Neuron 61, 541–555.

McBride HM, Neuspiel M, Wasiak S (2006). Mitochondria: more than just a powerhouse. Curr Biol 16, R551–R560.

Morlino G, Barreiro O, Baixauli F, Robles-Valero J, González-Granado JM, Villa-Bellosta R, Cuenca J, Sánchez-Sorzano CO, Veiga E, Martín-Cófreces NB, Sánchez-Madrid F (2014). Miro-1 links mitochondria and microtubule Dynein motors to control lymphocyte migration and polarity. Mol Cell Biol 34, 1412–1426.

Nguyen TT, Oh SS, Weaver D, Lewandowska A, Maxfield D, Schuler MH, Smith NK, Macfarlane J, Saunders G, Palmer CA, et al. (2014). Loss of Miro1-directed mitochondrial movement results in a novel murine model for neuron disease. Proc Natl Acad Sci USA 111, E3631–E3640.

Niescier RF, Chang KT, Min K-T (2013). Miro, MCU, and calcium: bridging our understanding of mitochondrial movement in axons. Front Cell Neurosci 7, 148.

Niethammer P, Kueh HY, Mitchison TJ (2008). Spatial patterning of metabolism by mitochondria, oxygen, and energy sinks in a model cytoplasm. Curr Biol 18, 586–591.

Nikolaisen J, Nilsson LIH, Pettersen IKN, Willems PHGM, Lorens JB, Koopman WJH, Tronstad KJ (2014). Automated quantification and integrative analysis of 2D and 3D mitochondrial shape and network properties. PloS One 9, e101365.

Osellame LD, Blacker TS, Duchen MR (2012). Cellular and molecular mechanisms of mitochondrial function. Best Pract Res Clin Endocrinol Metab 26, 711–723.

Pilling AD, Horiuchi D, Lively CM, Saxton WM (2006). Kinesin-1 and dynein are the primary motors for fast transport of mitochondria in drosophila motor axons. Mol Biol Cell 17, 2057–2068.

Quintana A, Hoth M (2012). Mitochondrial dynamics and their impact on T cell function. Cell Calcium 52, 57–63.

Ridley AJ, Schwartz MA, Burridge K, Firtel RA, Ginsberg MH, Borisy G, Parsons JT, Horwitz AR (2003). Cell migration: Integrating signals from front to back. Science 302, 1704–1709.

Riedl J, Crevenna AH, Kessenbrock K, Yu JH, Neukirchen D, Bista M, Bradke F, Jenne D, Holak TA, Werd Z, et al. (2008). Lifeact: a versatile marker to visualize F-actin. Nat Methods 5, 605–607.

Rivadeneira DB, Caino MC, Seo JH, Angelin A, Wallace DC, Languino LR, Altieri DC (2015). Survivin promotes oxidative phosphorylation, subcellular mitochondrial repositioning, and tumor cell invasion. Sci Signal 8, ra80.

Saotome M, Safiulina D, Szabadkai G, Das S, Fransson Å, Aspenstrom P, Rizzuto R, Hajnóczky G (2008). Bidirectional Ca2+-dependent control of mitochondrial dynamics by the Miro GTPase. Proc Natl Acad Sci USA 105, 20728–20733.

Saxton WM, Hollenbeck PJ (2012). The axonal transport of mitochondria. J Cell Sci 125, 2095–2104.

Schwarz TL (2013). Mitochondrial trafficking in neurons. Cold Spring Harb Perspect Biol 5, a011304–a011304.

Smith MA, Blankman E, Deakin NO, Hoffman LM, Jensen CC, Turner CE, Beckerle MC (2013). LIM domains target actin regulators paxillin and zyxin to sites of stress fiber strain. PLoS One 8, e69378.

Soubannier V, McBride HM (2009). Positioning mitochondrial plasticity within cellular signaling cascades. Biochim Biophys Acta 1793, 154–170.

Stowers RS, Megeath LJ, Górska-Andrzejak J, Meinertzhagen IA, Schwarz TL (2002). Axonal transport of mitochondria to synapses depends on Milton, a novel Drosophila protein. Neuron 36, 1063–1077.

Tanaka Y, Kanai Y, Okada Y, Nonaka S, Takeda S, Harada A, Hirokawa N (1998). Targeted disruption of mouse conventional kinesin heavy chain, kif5B, results in abnormal perinuclear clustering of mitochondria. Cell 93, 1147–1158.

Tantama M, Martínez-François JR, Mongeon R, Yellen G (2013). Imaging energy status in live cells with a fluorescent biosensor of the intracellular ATP-to-ADP ratio. Nat Commun 4, 2550.

Trepat X, Chen Z, Jacobson K (2012). Cell migration. Compr Physiol 2, 2369–2392.

Van Horssen R, ten Hagen TLM (2011). Crossing barriers: the new dimension of 2D cell migration assays. J Cell Physiol 226, 288–290.

Wang X, Schwarz TL (2009). The mechanism of Ca2+ -dependent regulation of kinesin-mediated mitochondrial motility. Cell 136, 163–174.

Wang Y, Zang QS, Liu Z, Wu Q, Maass D, Dulan G, Shaul PW, Melito L, Frantz DE, Kilgore JA, et al. (2011). Regulation of VEGF-induced endothelial cell migration by mitochondrial reactive oxygen species. Am J Physiol Cell Physiol 301, C695–C704.

Wong IY, Javaid S, Wong EA, Perk S, Haber DA, Toner M, Irimia D (2014). Collective and individual migration following the epithelial-mesenchymal transition. Nat Mater 13, 1063–1071.

Zaidel-Bar R, Cohen M, Addadi L, Geiger B (2004). Hierarchical assembly of cell–matrix adhesion complexes. Biochem Soc Trans 32, 416–420.

Zhao J, Zhang J, Yu M, Xie Y, Huang Y, Wolff DW, Abel PW, Tu Y (2013). Mitochondrial dynamics regulates migration and invasion of breast cancer cells. Oncogene 32, 4814–4824.

Zhu JY, Abate M, Rice PW, Cole CN (1991). The ability of simian virus 40 large T antigen to immortalize primary mouse embryo fibroblasts cosegregates with its ability to bind to p53. J Virol 65, 6872–6880.